



Surface-modified anatase nanocrystalline building blocks for constructing catalytically highly active nanoporous titania materials

Chia-Hsiu Chen^a, Chun-Hsia Liu^a, Yu-Chung Su^a, Chia-Min Yang^{a,b,*}

^a Department of Chemistry, National Tsing Hua University, Hsinchu 30013, Taiwan

^b Frontier Research Center on Fundamental and Applied Sciences of Matters, National Tsing Hua University, Hsinchu 30013, Taiwan

ARTICLE INFO

Article history:

Received 12 January 2012

Received in revised form 14 April 2012

Accepted 22 April 2012

Available online 26 April 2012

Keywords:

Anatase nanocrystal

Surface modification

Surfactant-directed assembly

Photodegradation

Epoxidation

ABSTRACT

Anatase nanocrystals with controlled size, shape and modified surface have been prepared and applied as nanocrystalline building blocks for surfactant-directed spontaneous assembly in aqueous solution. The nanocrystals were synthesized in a mixture of titanium tetrachloride and benzyl alcohol with the addition of pyridine as a modifying ligand. It was found that pyridine retarded the growth of anatase nanocrystals, preferentially along the *c* axis, and its addition resulted in nanocrystals with higher percentage of the high-energy {001} facets. Moreover, the nanocrystals were modified with pyridine chemisorbed at surface acid sites that were most likely to be associated to the five-coordinated titanium atoms. The pyridine-modified anatase nanocrystals interacted with sodium dodecyl sulfate in acidic aqueous solution, causing a spontaneous surfactant-directed assembly. After calcination, the surfactant-free nanoporous material exhibited high anatase crystallinity, high surface area, uniform mesoporosity and preferred surface properties. Owing to the textural and surface properties, the assembled material exhibited excellent catalytic activities in the photodegradation of methylene blue and in the epoxidation of cyclohexene with hydrogen peroxide as compared to reference titania samples.

© 2012 Elsevier B.V. All rights reserved.

1. Introduction

Titanium dioxide (TiO₂, or titania) is a low-cost, highly stable and wide band-gap semiconductor material. It has unique phase-dependent, crystallinity-dependent and facet-dependent properties [1–6] and exhibits excellent catalytic performance in energy- and environment-related applications [1–3,7–11]. There is no doubt that further improvement of the catalytic activity of titania materials relies on the development of new preparation methods to produce highly crystalline and high-surface-area materials with controlled surface properties.

High-surface-area mesostructured titania materials can be prepared by applying the evaporation-induced self-assembly (EISA) process using soft templates (e.g. surfactants and polymers) or hard templates (e.g. porous silica, porous carbon and polymer beads) [12–21]. However, the as-made materials are usually amorphous or with low crystallinity. Further crystallization by heat treatment often results in collapse of nanometer-sized pores and notable decrease in surface area, unless the hard template could support the mesostructure at elevated temperatures [18,21]. Alternatively, crystalline and high-surface-area titania and other metal

oxides can be fabricated by the surfactant-directed assembly of preformed nanocrystalline building blocks (NBBs) [11,22–28]. For the surfactant-directed assembly, the preformed NBBs with controlled size and shape need to form stable suspension prior to the assembly process. Moreover, the NBBs need to interact with surfactant molecules to initiate the assembly process. For the process involving strong surfactant–NBB interactions, spontaneous surfactant-directed assembly would take place. Otherwise, one needs to apply EISA if the interactions are relatively weak. Spontaneous surfactant-directed assembly provides more versatile control over the textural properties of the materials than EISA. However, the interactions between various types of surfactants and titania and other metal oxide NBBs are generally too weak to induce spontaneous assembly [11,24–27]. Obviously, the ability to modulate the surface properties of titania NBBs is crucial not only for achieving their spontaneous assembly with surfactants but also for improving the catalytic activities of the assembled materials.

Herein we report an efficient preparation of anatase-phase titania NBBs with controlled size and shape and modified surface properties for spontaneous anionic surfactant-directed assembly in aqueous solution. We applied the synthesis system of titanium tetrachloride (TiCl₄) and benzyl alcohol (BA) to synthesize monodisperse anatase NBBs [29–32]. The synthesis system has also been applied for surface functionalization of anatase nanocrystals with a variety of ligands in order to render the nanocrystals good solubility in water or in organic solvents [33–35]. Inspired by these

* Corresponding author at: Department of Chemistry, National Tsing Hua University, Hsinchu 30013, Taiwan. Tel.: +886 3 5731282; fax: +886 3 516552.

E-mail address: cmyang@mx.nthu.edu.tw (C.-M. Yang).

studies, we attempted to apply ligand-assisted nonaqueous synthesis to prepare anatase NBBs for spontaneous surfactant-directed assembly. The ligand we chose was pyridine, a relatively weak base and also a relatively weak ligand as compared to the ligands used in previous reports [33–35]. We found that the presence of pyridine modulated the size and shape of anatase nanocrystals by preferentially retarding crystal growth along the *c* axis, resulting in nanocrystals with higher percentage of the high-energy {001} facets. Moreover, we found that the surface of the nanocrystals was modified with pyridine molecules that were most likely chemisorbed at the five-coordinated Ti atoms. Remarkably, the pyridine-modified anatase NBBs interacted with sodium dodecyl sulfate (SDS) in acidic aqueous solution, causing a spontaneous precipitation of the assembly product. After calcination, the assembled material was applied as a catalyst for photodegradation of model pollutant and liquid-phase olefin epoxidation, the two test reactions chosen in this study. As compared to reference titania samples, the material showed excellent catalytic activities for both the reactions owing to its high crystallinity, high surface area, uniform mesoporosity and preferred surface properties.

2. Experimental

2.1. Materials synthesis

In a typical synthesis of anatase nanocrystals, TiCl_4 (1.0 M dichloromethane solution, 9.2 mL) was slowly added to BA (20.0 mL, dried over Molecular Sieve 4A and stored in a glove box) under vigorous stirring in an inert atmosphere at room temperature. The reaction is violent and caution should be taken. Pyridine was added to the solution, and the synthesis mixture was further stirred for 10 min and was then transferred and sealed in a Teflon reaction vessel. The molar composition was 1 TiCl_4 :*x* pyridine:20 BA. The mixture was subjected to microwave heating ($10^\circ\text{C min}^{-1}$ heating ramp) at 120°C for 1 h using a CEM MARS microwave digestion system operating at a frequency of 2.45 GHz. The resulting suspension was centrifuged, and the precipitate was thoroughly washed three times with ethanol. The solvent was removed by centrifugation after each washing step. The collected product was dried in air at 60°C . The samples are designated as Px, where *x* denotes the molar ratio of pyridine to TiCl_4 .

For the surfactant-directed assembly, anatase nanocrystals were poured into an aqueous solution of SDS and HCl. The molar composition was 1 TiO_2 :0.125 SDS:0.4 HCl:100 H_2O . The mixture was stirred for 30 min at room temperature. The precipitate was filtered, washed with water and ethanol, and finally dried in air at 60°C . The sample was calcined at 400°C for 3 h to remove the surfactant and other organic moieties.

2.2. Characterization

X-ray diffraction (XRD) patterns were measured on a Mac Science 18MPX diffractometer using $\text{Cu K}\alpha$ radiation as X-ray source. Transmission electron microscopic (TEM) images were recorded on a JEOL JEM-3000F electron microscope operating at 300 kV and a JEOL JEM-2100 electron microscope operating at 200 kV. Scanning electron microscopic (SEM) images were obtained with a field emission JEOL JSM-7000F microscope operating at 10 kV. Fourier-transform infrared (FT-IR) spectra were measured using a Nicolet 6700 spectrometer. Liquid-state ^1H NMR experiments were performed in a Bruker AC300 spectrometer with CDCl_3 as a solvent. Nitrogen physisorption isotherms were measured at 77 K using a Quantachrome Autosorb-1-MP instrument. Pore diameters and pore size distributions were calculated from the desorption branch using the Barrett-Joyner-Halenda (BJH) method. Thermogravimetric

analysis (TGA) and differential thermoanalysis (DTA) data were obtained using a Linseis STA PT1600 thermoanalyzer in an air flow (100 mL min^{-1}) with a heating rate of $10^\circ\text{C min}^{-1}$. Degree of dispersion and isoelectric points of TiO_2 samples were measured at 25°C using a 90Plus/BI-Zeta Analyzer by Brookhaven Instruments. UV–visible absorption spectra were recorded on a JASCO V-650 spectrophotometer equipped with a diffuse reflection accessory.

2.3. Catalytic studies

For the studies of photodegradation of methylene blue (MB), an aqueous solution of MB ($1.22 \times 10^{-5}\text{ M}$) was prepared and the solution pH was adjusted to 6.5 to prevent possible bleaching of the dye by reduction during the reaction. A TiO_2 catalyst (25 mg) was dispersed into the solution (200 mL). The mixture was stirred in the dark to reach adsorption equilibrium of MB. The amount of the adsorbed dye molecules was estimated from the decrease of the optical absorbance at a wavelength of 665 nm. The suspension was then irradiated by low-power (1.6 mW cm^{-2}) UV light from an Oriel 150 W xenon lamp, and the photodegradation proceeded under aerobic (oxygen-saturated) conditions. The UV–visible spectra of the MB solutions were obtained using a JASCO V-650 UV–visible spectrophotometer. The TiO_2 sample was removed by filtration prior to optical measurements.

For the epoxidation of cyclohexene, a TiO_2 catalyst (20 mg) was added to a solution of cyclohexene (0.5 mL) in *tert*-butanol (5 mL) in a glass flask fitted with a reflux condenser. The mixture was vigorously stirred and heated to 60°C . 30 wt% aqueous hydrogen peroxide (H_2O_2) (0.1 mL) was then added to the mixture to start the reaction. The reaction was performed at 60°C for 3 h, and the aliquot was withdrawn from the mixture, filtered, and finally analyzed on a gas chromatograph (Shimadzu GC-2014) equipped with a flame ionization detector.

3. Results and discussion

3.1. Synthesis and characterization of anatase nanocrystals

The presence of pyridine was found to retard the materials growth in the synthesis system of BA and TiCl_4 and modulated the size and shape of the resulting anatase NBBs. The synthesis with a pyridine-to- TiCl_4 ratio (*x*) of 1 (resulting in sample P1.0) gave an excellent yield (>95% with respect to TiCl_4) almost identical to that for the pyridine-free synthesis (resulting in sample P0). The yield decreased to 70% for P2.0 and 48% for P2.3, and no solid products could be collected with $x \geq 2.5$.

Fig. 1 shows the powder XRD patterns of the samples. All the diffraction peaks can be assigned to the anatase phase without any indication of other crystalline polymorphs as byproducts. The peaks are relatively broad due to the nanosize of the crystals. By applying Scherrer equation the particle sizes of the samples were estimated from the (101) reflection of anatase [31]. With the addition of pyridine, the particle size of anatase nanocrystals decreased from 7.8 nm for the sample P0 to 5.7 nm, 4.1 nm and 3.0 nm for P1, P2 and P2.3, respectively. Clearly, pyridine retarded the anatase growth to produce even smaller anatase nanocrystals. Moreover, Polleux et al. have shown that the relative intensities of the (004) and (200) reflections, representing the *c* and *a* axes, respectively, may be a good indication of the degree of anisotropic growth of anatase nanocrystals [35]. For P0, the (004) reflection is more intense and sharper than the (200) reflection, revealing an extended crystalline domain along the *c* axis, which is typical for anatase nanocrystals with a preferred growth in this direction [31–35]. The (004) reflection becomes broader and less intense than the (200) reflection with increasing *x*, and for P2.3 the (004) reflection could

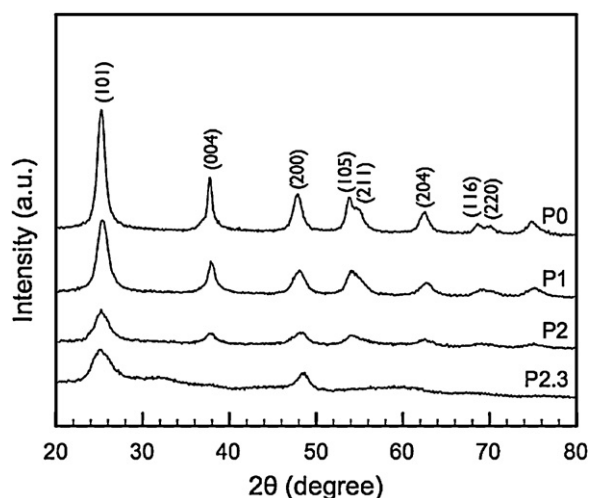


Fig. 1. Powder XRD patterns of the TiO_2 samples.

be hardly discerned. Therefore, the results further indicate that the anisotropic growth along the c axis was suppressed leading to a less elongated particle shape of anatase nanocrystals. The suppression by pyridine was also observed for the anatase nanocrystals synthesized with conventional heating in an oil bath, but longer reaction time and more pyridine were needed to reach similar degree of suppression (see Fig. S1 of the Supplementary Information).

The TEM data coincided well with the XRD results. Fig. 2 shows the TEM images of P0 and P2.3. The anatase nanocrystals in P0 have a shape of slightly truncated bipyramid with crystalline domain extended along the c axis. The lattice fringes seen in the high-resolution image (Fig. 2b) can be well assigned to the $\{101\}$

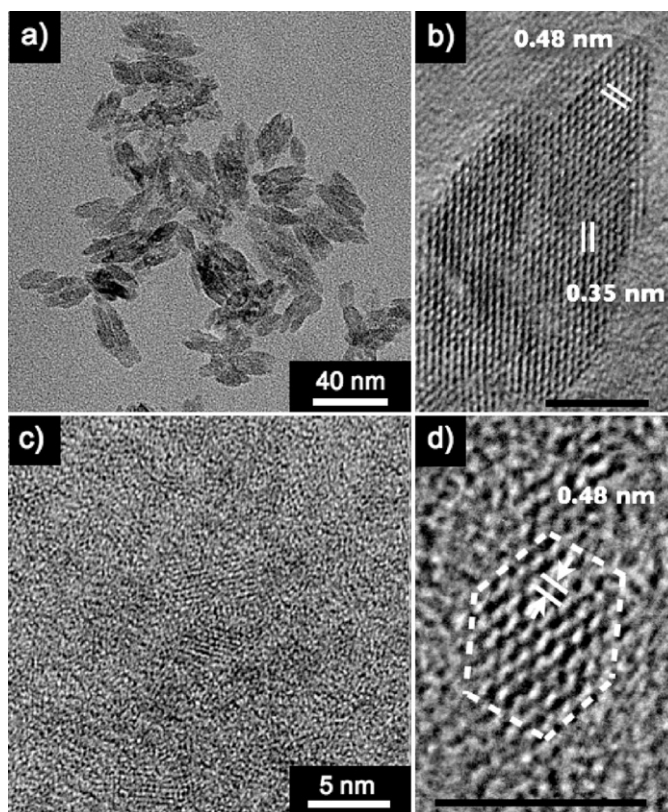


Fig. 2. TEM images of P0 (a, b) and P2.3 (c, d). Scale bars in (b) and (d) correspond to 5 nm.

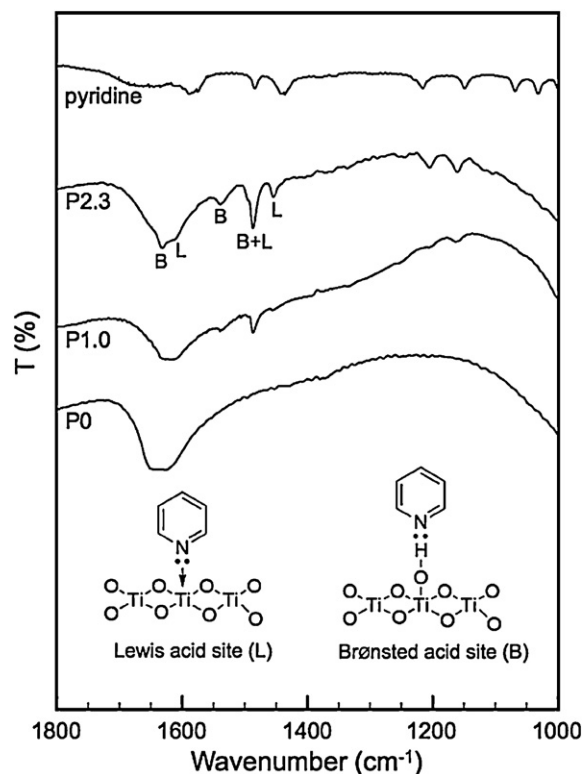


Fig. 3. FT-IR spectra of P0, P1.0, P2.3 and pyridine. The pyridine molecules adsorbed at Lewis and Brønsted acid sites on the surface of anatase nanocrystals are depicted.

(d -spacing of 0.35 nm) and $\{002\}$ (d -spacing of 0.48 nm) planes of anatase phase, and the observed interfacial angle ($\sim 68^\circ$) is nearly identical to the theoretical value for anatase [4]. The anisotropic growth of anatase nanocrystals may be associated with the preferential adsorption of BA on the $\{101\}$ faces, as suggested by Niederberger and co-workers [33–35]. On the other hand, the anatase nanocrystals in P2.3 are smaller and well dispersed. They have a shape similar to that for the nanocrystals in P0 but exhibit a higher degree of truncation along the c axis, and the lattice fringes corresponding to the $\{002\}$ planes are observed to be parallel to the truncation surface (cf. Fig. 2d). Based on the crystal shape of anatase and the degree of truncation for the anatase nanocrystals in the two samples, [4,6] we could estimate the percentages of $\{001\}$ facets to be 2% and 17% for in P0 and P2.3, respectively.

The influence of pyridine on the reaction mechanism in the nonaqueous TiCl_4/BA system was also investigated by analyzing the final reaction solutions by ^1H NMR. The formation of anatase nanocrystals in TiCl_4/BA proceeds through alkyl halide elimination and ether elimination, the former being the main reaction pathway due to stabilization of the transient carbocation by the phenyl ring of BA [30,32]. Garnweitner and Niederberger found that the ligands or surface modifiers bearing amino and/or hydroxyl groups significantly alter the reaction pathways, resulting in dramatic change in the ratio of the two reaction byproducts [32]. In our case, however, we found that for the syntheses with or without pyridine, the final reaction solutions contained benzyl chloride and benzyl ether with nearly the same molar ratio of 3:1 (see Fig. S2 in the Supplementary Information). The results suggest that pyridine acted as a weak ligand in the nonaqueous synthesis system and did not affect the reaction mechanism for the formation of anatase nanocrystals.

On the other hand, FT-IR investigation revealed that the addition of pyridine in TiCl_4/BA significantly modified the surface properties of the resulting anatase nanocrystals. As shown in Fig. 3, P0 exhibited a relatively broad peak at $1620\text{--}1650\text{ cm}^{-1}$ in the spectra that

may be assigned to the angular bending of the adsorbed water. For P1 and P2.3, additional peaks of pyridine appeared in their spectra. As compared with the spectrum of pyridine, the peaks are shifted to higher energy and can be grouped into two that are attributed to the pyridine molecules chemisorbed at different acid sites on the anatase nanocrystals [36,37]. The peaks at 1455 and 1611 cm^{-1} may be attributed to the pyridine molecules interacted with the Lewis acid sites, while the peaks at 1541 and 1633 cm^{-1} are from those protonated by the Brønsted acid sites. The vibration of the adsorbed pyridine on both sites gives rise to the peak at 1488 cm^{-1} . The chemisorbed state of pyridine in P2.3 is further confirmed by the much higher desorption/decomposition temperature of the pyridine in P2.3 (350–450 $^{\circ}\text{C}$) than the boiling point ($\sim 150^{\circ}\text{C}$) of the molecule (cf. the TGA curve of P2.3 shown in Fig. S3 in the Supplementary Information). The presence of the chemisorbed pyridine molecules and the corresponding acid sites highlights the uniqueness of the pyridine-assisted nonaqueous synthesis of anatase nanocrystals since the surface acidity of pure titania materials is generally too weak to interact with pyridine [37]. The amount of the chemisorbed pyridine increased with increasing the pyridine-to- TiCl_4 ratio in the synthesis mixture, and P2.3 contained around 13 wt% of chemisorbed pyridine (cf. Fig. S3 in the Supplementary Information), corresponding to a pyridine-to-titanium ratio of around 1:5. As for the nature of the acid sites, they are most likely to be associated to the coordinately unsaturated (five-coordinate) surface Ti (Ti_{5c}) atoms: The Ti_{5c} atoms are themselves Lewis acid sites, and they may react with water, most probably during the washing steps, to generate the Brønsted acid sites (i.e. the surface-bound hydroxyl groups or titanol groups) [37]. Since the {001} facets feature 100% Ti_{5c} atoms, whereas 50% of the surface Ti atoms are five-coordinated for the {101} facets, the surface density of the chemisorbed pyridine molecules on the two truncated {001} surfaces of anatase nanocrystals should be higher than that for the {101} surfaces if the Ti_{5c} atoms on both types of facets interact similarly with pyridine. The difference in the percentage of Ti_{5c} atoms may also explain why pyridine preferentially suppressed the growth of anatase nanocrystals along the *c* axis, as indicated by XRD and TEM.

3.2. Surfactant-directed assembly of anatase nanocrystals

The dispersion of the samples P0 and P2.3 in water was observed prior to the surfactant-directed assembly. We found it difficult to disperse P0 in water, and hours of ultrasonic agitation were necessary to form a completely dispersed and stable colloidal solution. The poor water dispersibility of the anatase nanocrystals synthesized in TiCl_4/BA may be attributed to the presence of the organics remained on the surface [33–35]. On the other hand, P2.3 could be easily dispersed in water, during which the chemisorbed pyridine molecules in P2.3 were desorbed and the corresponding Ti_{5c} atoms interacted with water, a stronger nucleophile than pyridine, to form titanol groups. The desorption of pyridine was evidenced by the FT-IR spectrum of the water-washed P2.3 shown in Fig. 4, in which all the peaks of the chemisorbed pyridine disappear. The isoelectric points of the colloidal solution of P0 and P2.3 were 5.6 and 5.4, respectively.

The surfactant-directed assemblies of anatase NBBs were performed in aqueous solution of anionic surfactant SDS at pH ~ 0.6 . Whereas P0 remained a stable suspension in SDS solution, remarkably, the addition of P2.3 into SDS solution caused a spontaneous precipitation of a white solid (denoted as P2.3-SDS) that could be collected by simple filtration. The SEM images in Fig. 5 show that the anatase NBBs, assembled with SDS, formed uniform aggregates with sizes of 100–500 nm that further agglomerate into micrometer-sized particles. Thermal analysis data (Fig. S4 in the Supplementary Information) suggest that

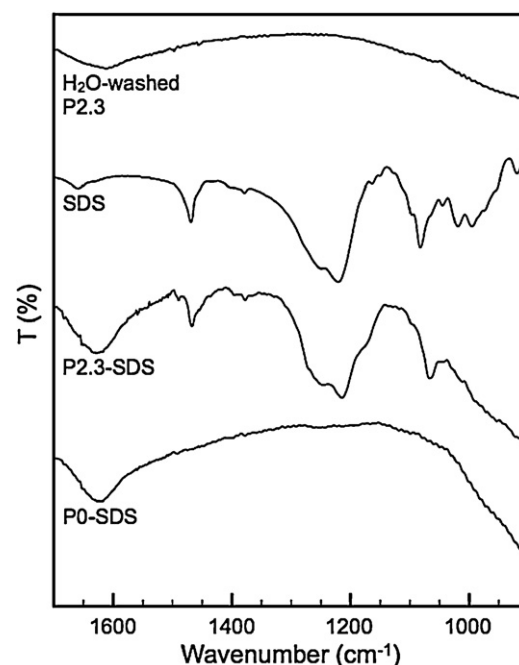


Fig. 4. FT-IR spectra of water-washed P2.3, SDS, P2.3-SDS and P0-SDS.

P2.3-SDS was highly hydrated and contained around 18 wt% of water (corresponding to the weight loss up to 200 $^{\circ}\text{C}$) and 24 wt% of SDS (corresponding to the weight loss between 200 and 400 $^{\circ}\text{C}$). The yield was around 95% based on the weight of titania in the sample. Moreover, as shown in Fig. 4, while the FT-IR spectrum of P2.3-SDS shows all the peaks of the surfactant, including the peaks of the sulfate head group (between 1255 cm^{-1} and 1000 cm^{-1} for stretching vibration of $-\text{OSO}_3-$ groups and for SO_3 vibrations) and the dodecyl group (1460, 1400 and 1380 cm^{-1} for C–H vibrations), the peaks of the sulfate head group are slightly shifted to lower energy for about 4–14 cm^{-1} as compared to those in the spectrum of SDS. On the contrary, we found that no SDS molecules were adsorbed on P0, as indicated by the FT-IR spectrum of the sample collected from the suspension of P0 in SDS by centrifugation (denoted as P0-SDS in Fig. 4). Based on these observations and the characterization of anatase NBBs, we believe that the spontaneous SDS-directed assembly of anatase NBBs in P2.3 should be associated with strong SDS–NBB interactions. As schematically shown in Fig. 6, once the pyridine-modified anatase NBBs were dispersed in the SDS solution, the ligand molecules would be nucleophilically substituted by water and the Ti_{5c} atoms would become surface titanol

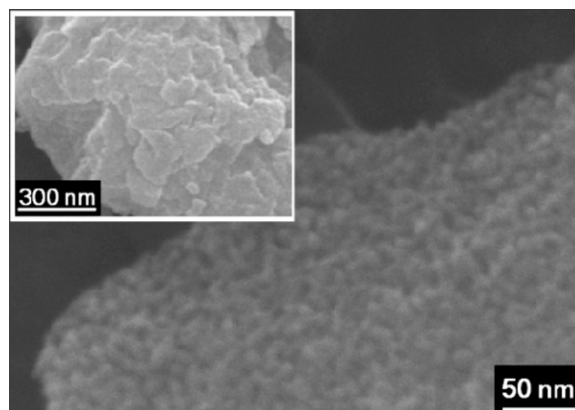


Fig. 5. SEM image of P2.3-SDS-C.

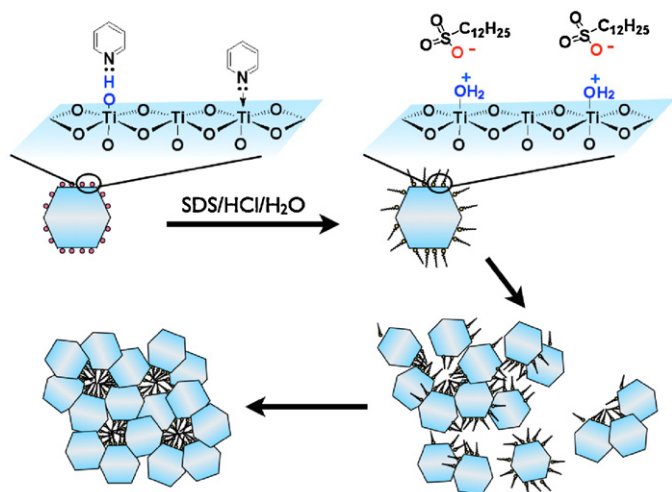


Fig. 6. Schematic representation of the spontaneous SDS-directed assembly of anatase NBBs.

groups. The titanol groups get protonated under acidic conditions, and the positively charged surface groups may interact with SDS through Coulomb attraction. The aggregation of surfactant molecules would then induce the assembly of NBB leading to the precipitation of solid product. As mentioned in Section 1, the reported surfactant-directed assemblies of oxide NBBs often involve relatively weak organic/inorganic interactions and either the method of EISA has to be applied or the assembly products have to be collected by centrifugation [11,24–27]. Compared to these reports, the key to the spontaneous surfactant-directed assembly observed in this study should be the anatase NBBs with controlled size, shape and, most importantly, surface properties.

The wide-angle XRD pattern of P2.3-SDS (Fig. 7a) is nearly identical to that of P2.3 (cf. Fig. 1), suggesting that the shape, size and crystallinity of the anatase nanocrystals were retained in P2.3-SDS. The sample exhibits a broad reflection centered at 2.1° , corresponding to an inter-nanoparticle distance of 4.5 nm. Although the small-angle reflection suggests some degree of mesoscopic order [11,15,16,23,27] in P2.3-SDS, the inter-nanoparticle distance is too short for a regular organization of NBBs and surfactant micelles. Since the NBBs are rigid, the result implies a denser packing of SDS in P2.3-SDS than that in regular micellar structure. This might be probably due to the fact that the SDS–NBB interactions are stronger than the hydrophobic interactions between surfactant molecules, and the aggregation of NBBs might force SDS molecules to change their arrangement during the assembly process. The surfactant in P2.3-SDS was removed by calcination at 400°C , resulting in sample P2.3-SDS-C. The anatase nanocrystals in this sample are smaller than those in the reference sample P2.3-C prepared by calcining P2.3 at 400°C , suggesting that the surfactant molecules may retard particle growth during calcination. Furthermore, P2.3-SDS-C displays a type IV nitrogen physisorption isotherm with a sharp H1-type hysteresis loop corresponding to the filling of channel-type mesopores with narrow pore size distribution, but P2.3-C exhibits a low sorption capacity and a wide loop in the isotherm (cf. Fig. 7b). Obviously, P2.3-SDS-C has much higher surface area, more uniform mesopores and larger pore volume than P2.3-C does (cf. Table 1). P2.3-SDS-C also exhibits a small-angle reflection at 0.6° (cf. Fig. 7a). The corresponding inter-nanoparticle distance (14.7 nm) is very close to the sum of the estimated NBB size (8.0 nm) and mesopore diameter (6.4 nm), but it is much longer than that for P2.3-SDS. It seems that the assembled NBBs in P2.3-SDS experienced rather uniform collapse during the calcination to result in P2.3-SDS-C with uniform mesoporosity. Consistent with XRD

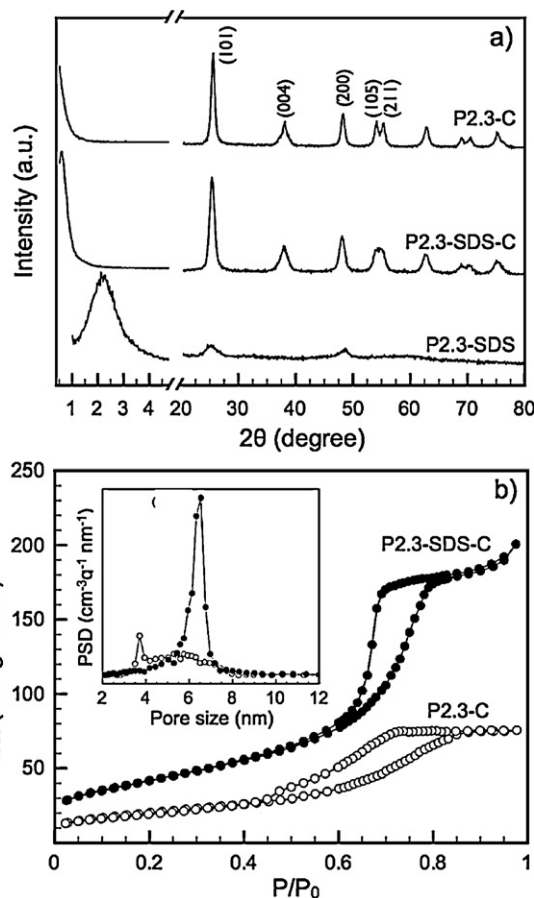


Fig. 7. (a) Powder XRD patterns of P2.3-SDS, P2.3-SDS-C and P2.3-C. (b) Nitrogen physisorption isotherms and the corresponding pore size distributions of P2.3-SDS-C and P2.3-C.

and nitrogen physisorption results, the TEM images of P2.3-SDS-C, as shown in Fig. 8, reveal simultaneously lattice fringes of anatase nanocrystals with sizes of 7–9 nm and relatively uniform worm-like mesopores.

3.3. Photodegradation of methylene blue

The catalytic performances of P2.3-SDS-C in photodegradation of pollutants and in liquid-phase olefin epoxidation with H_2O_2 , two of the most important reactions of titania-based catalysts, were examined. Commercially available Degussa P25 and ISK (Ishihara Sangyo Kaisha) ST-21 were applied as reference catalysts. In addition, two calcined samples derived from P0 and P2.3, denoted as P0-C and P2.3-C, respectively, were also prepared and tested for the reactions in order to see the influence of surface and textural properties on the catalytic performance. P2.3 was washed by water before calcination to desorb pyridine molecules, and a calcination temperature of 400°C was chosen for all the three samples to

Table 1
Textural properties of selected titania samples.^a

Samples	D_A (nm)	S_{BET} ($\text{m}^2 \text{g}^{-1}$)	d_m (nm)	V_t ($\text{cm}^3 \text{g}^{-1}$)
P2.3-SDS-C	8.0	152	6.4	0.34
P0-C	11.0	64	5.5	0.18
P2.3-C	10.5	72	5.3	0.12
P25	20.5	51	23	0.23
ST-21	20.2	61	20	0.25

^a D_A : particle size of anatase phase; S_{BET} : BET surface area; d_m : mesopore diameter; V_t : total pore volume.

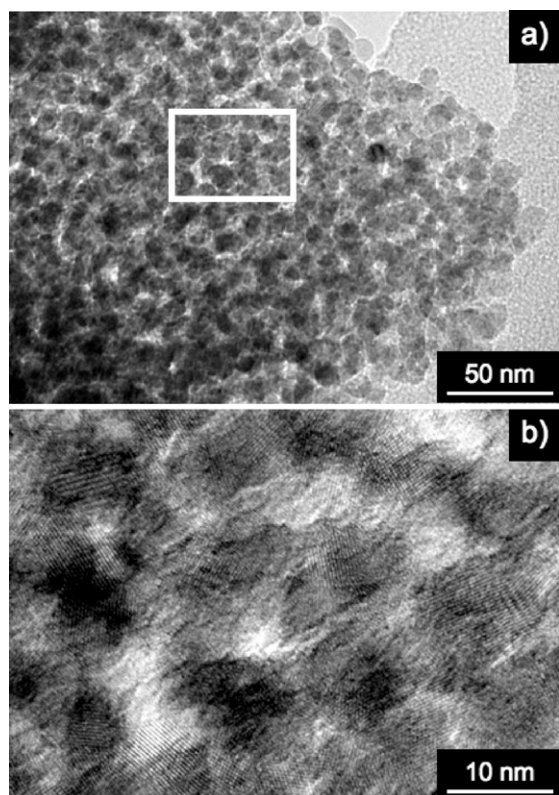


Fig. 8. (a) TEM image of P2.3-SDS-C. (b) An enlarged image from the rectangular area in (a) showing the lattice fringes of anatase nanocrystals.

completely decompose the remaining organics without significantly facilitating condensation of titanol groups on anatase surface.

For the photodegradation studies, methylene blue (MB) was chosen because it is often used as a test model pollutant in semiconductor photocatalysis [2,3,38,39]. All the samples showed very little MB adsorption so that the effect of dye adsorption could be excluded. For the oxidative photodegradation reactions, the MB solution was oxygen-saturated at pH 6.5 to avoid the reduction of the dye, and a low-power UV irradiation was applied to prevent possible multi-photon processes or serious absorption of MB [38,39]. Upon UV irradiation, the concentration of MB (determined from the optical absorbance at 665 nm) in the solution containing a titania photocatalyst decreased over time (cf. Fig. S5 in the Supplementary Information). After subtracting the amount of the self-degradation of the photoexcited dye (i.e. the amount of bleached dye in the absence of catalyst), we found that while only 13.2–16.8% of MB was bleached by P25 and ST-21 after two-hour UV irradiation, about 70.6% of the dye was degraded by P2.3-SDS-C within the same period of time. The other two samples also outperformed the commercial catalysts but showed smaller amount of dye degradation than P2.3-SDS-C (32.4% and 36.2% for P0-C and P2.3-C, respectively). The degradation profiles for all the catalysts could be fitted by a first-order kinetic model, and the derived apparent first-order rate constants were used to evaluate the photocatalytic activities of the samples. For the commercial titania catalysts, the rate constants were $1.3\text{--}1.5 \times 10^{-3} \text{ min}^{-1}$. ST-21 showed slightly better photoactivity than P25 probably due to its pure anatase phase in comparison to the mixed anatase–rutile phases of P25. Remarkably, P2.3-SDS-C exhibited a rate constant ($7.9 \times 10^{-3} \text{ min}^{-1}$) that was more than five times higher than those for P25 and ST-21 and about 2.4–2.6 times higher than those for P0-C ($3.0 \times 10^{-3} \text{ min}^{-1}$) and P2.3-C ($3.3 \times 10^{-3} \text{ min}^{-1}$). The much

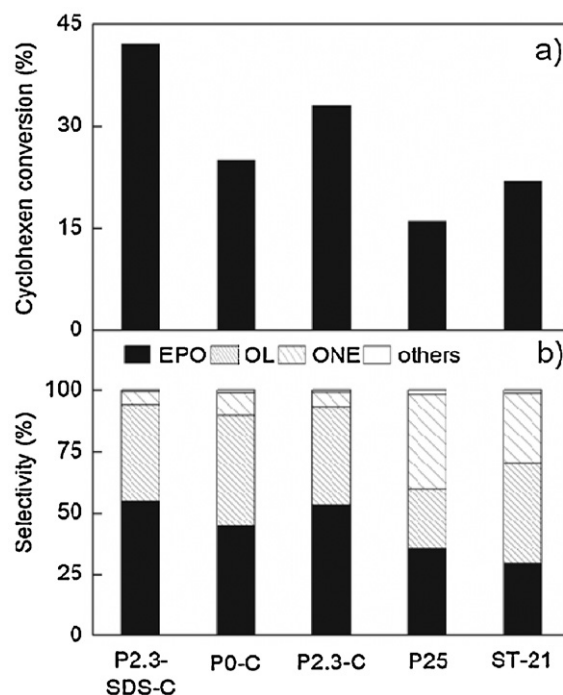


Fig. 9. Cyclohexene conversion (a) and product selectivities (b) for the titania catalysts. EPO: cyclohexene oxide; OL: cyclohex-2-en-1-ol; ONE: cyclohex-2-en-1-one.

enhanced photocatalytic activity for P2.3-SDS-C may be attributed to its high anatase crystallinity, high surface area and uniform mesoporosity.

3.4. Cyclohexene epoxidation with hydrogen peroxide

The five samples were also applied as catalysts for cyclohexene epoxidation with H_2O_2 . The reaction has been frequently performed to test the epoxidation activity of titanium-containing mesoporous silicas and zeolites [40–43] and titania-based materials [44,45]. The catalytic performance of all the samples is summarized in Fig. 9. The conversion of cyclohexene seems to be correlated to the textural properties of the samples. P2.3-SDS-C exhibited the highest cyclohexene conversion of 42%, much better than those for P25 and ST-21, the least active among all tested catalysts. For the other two samples, P2.3-C exhibited a higher conversion of 33% than P0-C did (25%). It seems that high surface area and uniform mesoporosity may facilitate reactant accessibility and surface reaction and therefore enhance the conversion of cyclohexene.

On the other hand, distinct product selectivities were observed for different catalysts. P2.3-SDS-C showed the highest cyclohexene oxide (EPO) selectivity of 54.8%. It was noted that P2.3-C exhibited similar product selectivities with those for P2.3-SDS-C and also showed high EPO selectivity. Compared to the two samples derived from P2.3, P0-C showed slightly lower EPO selectivity but higher selectivities for cyclohex-2-en-1-ol and cyclohex-2-en-1-one. The product selectivities for P25 and ST-21 were varied with relatively low selectivity of EPO. The distinct product selectivities may be associated to the surface properties of the titania samples. Cyclohexene epoxidation performed in *tert*-butanol- H_2O_2 system involves the formation of catalytically active *tert*-butyl peroxotitanium and peroxotitanium species by reacting *tert*-butyl hydroperoxide and H_2O_2 with surface titanol groups, respectively [40–45]. For the three samples derived from P2.3 and P0, both containing faceted anatase nanocrystals, the percentages of {001} and {101} facets and the density of surface titanol groups are

different. That fact that P2.3-SDS-C and P2.3-C, both derived from P2.3, gave very similar product distribution that was distinct from that for P0-C might imply possible facet-dependent and/or titanol density-dependent catalytic activities of anatase nanocrystals in epoxidation. To our best knowledge, such dependencies of catalytic performance of titania nanocrystals in epoxidation has never been observed, and further studies are necessary to verify it.

4. Conclusion

We have demonstrated a pyridine-assisted nonaqueous synthesis of anatase nanocrystals with controlled size, shape and surface properties. We found that pyridine retarded the growth of anatase phase, preferentially along the *c* axis, and its addition resulted in nanocrystals with higher percentage of the high-energy {001} facets. The surface of the nanocrystals was modified with pyridine molecules that were most likely chemisorbed at the five-coordinated Ti atoms. The pyridine-modified anatase nanocrystals interacted with sodium dodecyl sulfate in acidic aqueous solution, causing a spontaneous surfactant-directed assembly. After calcination, the surfactant-free nanoporous anatase material had high crystallinity, high surface area, uniform mesoporosity and preferred surface properties. Owing to the textural and surface properties, the assembled material exhibited excellent photodegradation and epoxidation activities as compared to reference titania samples.

Acknowledgement

We thank the National Science Council of Taiwan for the financial support under the contract nos. NSC98-2113-M-007-020-MY3 and NSC101-3113-P-008-001.

Appendix A. Supplementary data

Supplementary data associated with this article can be found, in the online version, at <http://dx.doi.org/10.1016/j.apcatb.2012.04.030>.

References

- [1] A.L. Linsebigler, G.Q. Lu, J.T. Yates, *Chemical Reviews* 95 (1995) 735–758.
- [2] A. Mills, R.H. Davies, D. Worsley, *Chemical Society Reviews* 22 (1993) 417–425.
- [3] X. Chen, S.S. Mao, *Chemical Reviews* 107 (2007) 2891–2959.
- [4] H.G. Yang, C.H. Sun, S.Z. Qiao, J. Zou, G. Liu, S.C. Smith, H.M. Cheng, G.Q. Lu, *Nature* 453 (2008) 634–638.
- [5] B.H. Wu, C.Y. Guo, N.F. Zheng, Z.X. Xie, G.D. Stucky, *Journal of the American Chemical Society* 130 (2008) 17563–17567.
- [6] Y.Q. Dai, C.M. Copley, J. Zeng, Y.M. Sun, Y.N. Xia, *Nano Letters* 9 (2009) 2455–2459.
- [7] A. Fujishima, K. Honda, *Nature* 238 (1972) 37–38.
- [8] B. Oregan, M. Gratzel, *Nature* 353 (1991) 737–740.
- [9] M. Gratzel, *Nature* 414 (2001) 338–344.
- [10] S.Y. Choi, M. Mamak, N. Coombs, N. Chopra, G.A. Ozin, *Advanced Functional Materials* 14 (2004) 335–344.
- [11] J.M. Szeifert, D. Fattakhova-Rohlfing, D. Georgiadou, V. Kalousek, J. Rathousky, D. Kuang, S. Wenger, S.M. Zakeeruddin, M. Gratzel, T. Bein, *Chemistry of Materials* 21 (2009) 1260–1265.
- [12] D.M. Antonelli, J.Y. Ying, *Angewandte Chemie International Edition* 34 (1995) 2014–2017.
- [13] P.D. Yang, D.Y. Zhao, D.I. Margolese, B.F. Chmelka, G.D. Stucky, *Nature* 396 (1998) 152–155.
- [14] C.J. Brinker, Y.F. Lu, A. Sellinger, H.Y. Fan, *Advanced Materials* 11 (1999) 579–585.
- [15] H.S. Yun, K. Miyazawa, H.S. Zhou, I. Honma, M. Kuwabara, *Advanced Materials* 13 (2001) 1377–1380.
- [16] G.J.D.A. Soler-Illia, A. Louis, C. Sanchez, *Chemistry of Materials* 14 (2002) 750–759.
- [17] D. Grosso, F. Cagnol, G.J.D.A. Soler-Illia, E.L. Crepaldi, H. Amenitsch, A. Brunet-Bruneau, A. Bourgeois, C. Sanchez, *Advanced Functional Materials* 14 (2004) 309–322.
- [18] A.H. Lu, F. Schüth, *Advanced Materials* 18 (2006) 1793–1805.
- [19] Y. Wan, H.F. Yang, D.Y. Zhao, *Accounts of Chemical Research* 39 (2006) 423–432.
- [20] S.W. Boettcher, J. Fan, C.K. Tsung, Q.H. Shi, G.D. Stucky, *Accounts of Chemical Research* 40 (2007) 784–792.
- [21] J. Lee, M.C. Orillall, S.C. Warren, M. Kamperman, F.J. DiSalvo, U. Wiesner, *Nature Materials* 7 (2008) 222–228.
- [22] C. Sanchez, G.J.D.A. Soler-Illia, F. Ribot, T. Lalot, C.R. Mayer, V. Cabuil, *Chemistry of Materials* 13 (2001) 3061–3083.
- [23] M.S. Wong, E.S. Jeng, J.Y. Ying, *Nano Letters* 1 (2001) 637–642.
- [24] J.Y. Chane-Ching, F. Cobo, D. Aubert, H.G. Harvey, M. Airiau, A. Corma, *Chemistry – A European Journal* 11 (2005) 979–987.
- [25] E.C. Mbamala, A. Ben-Shaul, S. May, *Biophysical Journal* 88 (2005) 1702–1714.
- [26] Z.D. Lu, M.M. Ye, N. Li, W.W. Zhong, Y.D. Yin, *Angewandte Chemie International Edition* 49 (2010) 1862–1866.
- [27] S.K. Das, M.K. Bhunia, A. Bhaumik, *Dalton Transactions* 39 (2010) 4382–4390.
- [28] M. Grzelczak, J. Vermant, E.M. Furst, L.M. Liz-Marzan, *ACS Nano* 4 (2010) 3591–3605.
- [29] A. Vioux, *Chemistry of Materials* 9 (1997) 2292–2299.
- [30] M. Niederberger, M.H. Bartl, G.D. Stucky, *Journal of the American Chemical Society* 124 (2002) 13642–13643.
- [31] M. Niederberger, G. Garnweitner, *Chemistry – A European Journal* 12 (2006) 7282–7302.
- [32] G. Garnweitner, M. Niederberger, *Journal of Materials Chemistry* 18 (2008) 1171–1182.
- [33] M. Niederberger, G. Garnweitner, F. Krumeich, R. Nesper, H. Colfen, M. Antonietti, *Chemistry of Materials* 16 (2004) 1202–1208.
- [34] J. Polleux, N. Pinna, M. Antonietti, M. Niederberger, *Advanced Materials* 16 (2004) 436–439.
- [35] J. Polleux, N. Pinna, M. Antonietti, C. Hess, U. Wild, R. Schlogl, M. Niederberger, *Chemistry – A European Journal* 11 (2005) 3541–3551.
- [36] O.M. Busch, W. Brijoux, S. Thomson, F. Schüth, *Journal of Catalysis* 222 (2004) 174–179.
- [37] X.C. Wang, J.C. Yu, P. Liu, X.X. Wang, W.Y. Su, X.Z. Fu, *Journal of Photochemistry and Photobiology A: Chemistry* 179 (2006) 339–347.
- [38] Y.C. Hsu, H.C. Lin, C.W. Lue, Y.T. Liao, C.M. Yang, *Applied Catalysis B: Environmental* 89 (2009) 309–314.
- [39] Y.C. Hsu, H.C. Lin, C.H. Chen, Y.T. Liao, C.M. Yang, *Journal of Solid State Chemistry* 183 (2010) 1917–1924.
- [40] T. Blasco, A. Corma, M.T. Navarro, J.P. Pariente, *Journal of Catalysis* 156 (1995) 65–74.
- [41] A. Corma, P. Esteve, A. Martinez, S. Valencia, *Journal of Catalysis* 152 (1995) 18–24.
- [42] T. Maschmeyer, F. Rey, G. Sankar, J.M. Thomas, *Nature* 378 (1995) 159–162.
- [43] N. Jappor, Q. Xia, T. Tatsumi, *Journal of Catalysis* 180 (1998) 132–141.
- [44] T. Sreethawong, Y. Yamada, T. Kobayashi, S. Yoshikawa, *Journal of Molecular Catalysis A: Chemical* 241 (2005) 23–32.
- [45] T. Sreethawong, Y. Yamada, T. Kobayashi, S. Yoshikawa, *Journal of Molecular Catalysis A: Chemical* 248 (2006) 226–232.